◆ Human Brain Mapping 38:5274–5291 (2017) ◆

Validation of Brain-Derived Signals in Near-Infrared Spectroscopy Through Multivoxel Analysis of Concurrent Functional Magnetic Resonance Imaging

Yoshiya Moriguchi,[1,2]* **Takamasa Noda**,[3,4] **Kosei Nakayashiki**,[3] **Yohei Takata**,[3] **Shiori Setoyama**,[5] **Shingo Kawasaki**,[6] **Yoshihiko Kunisato**,[7] **Kazuo Mishima**,[1] **Kazuyuki Nakagome**,[5,8] and **Takashi Hanakawa**[3,9]

[1]*Department of Psychophysiology, National Institute of Mental Health, National Center of Neurology and Psychiatry, 4-1-1, Ogawahigashi, Kodaira, Tokyo 187-8551, Japan*
[2]*Lundbeck Japan, Minato, Tokyo 105-0001, Japan*
[3]*Department of Advanced Neuroimaging, Integrative Brain Imaging Center, National Center of Neurology and Psychiatry, 4-1-1, Ogawahigashi, Kodaira, Tokyo 187-8551, Japan*
[4]*Clinical Optic Imaging Section, Department of Clinical Neuroimaging, Integrative Brain Imaging Center, National Center of Neurology and Psychiatry, 4-1-1, Ogawahigashi, Kodaira, Tokyo 187-8551, Japan*
[5]*Department of Psychiatry, National Center Hospital, National Center of Neurology and Psychiatry, 4-1-1, Ogawahigashi, Kodaira, Tokyo 187-8551, Japan*
[6]*Technical Support Group, Optical Topography Business Department, Business Promotion Division, Hitachi Medical Corporation, 2-1, Shintoyofuta, Kashiwa, Chiba 277-0804, Japan*
[7]*Department of Psychology, School of Human Sciences, Senshu University, 2-1-1, Higashi-Mita, Tama, Kawasaki, Kanagawa 214-8580, Japan*
[8]*National Institute of Mental Health, National Center of Neurology and Psychiatry, 4-1-1, Ogawahigashi, Kodaira, Tokyo 187-8551, Japan*
[9]*PRESTO, Japan Science and Technology Agency, Kawaguchi, Saitama 332-0012, Japan*

Abstract: Near-infrared spectroscopy (NIRS) is a convenient and safe brain-mapping tool. However, its inevitable confounding with hemodynamic responses outside the brain, especially in the frontotemporal head, has questioned its validity. Some researchers attempted to validate NIRS signals through concurrent measurements with functional magnetic resonance imaging (fMRI), but, counterintuitively, NIRS signals rarely correlate with local fMRI signals in NIRS channels, although both mapping techniques should measure the same hemoglobin concentration. Here, we tested a novel hypothesis that different *voxel*s within the scalp and the brain tissues might have substantially different hemoglobin absorption rates of near-infrared light, which

Additional Supporting Information may be found in the online version of this article.

Contract grant sponsor: Intramural Research Grant; Contract grant numbers: 20-3, 21-9, 24-10, 26-2, 26-3; Contract grant sponsor: Health and Labor Sciences Research Grants (Comprehensive Research on Disability, Health and Welfare)

*Correspondence to: Yoshiya Moriguchi; Department of Psychophysiology, National Institute of Mental Health, National Center of Neurology and Psychiatry, 4-1-1, Ogawahigashi, Kodaira, 187-8551 Tokyo, Japan. E-mail: ymorigu@ncnp.go.jp

Received for publication 18 January 2017; Revised 7 July 2017; Accepted 11 July 2017.

DOI: 10.1002/hbm.23734

Published online 19 July 2017 in Wiley Online Library (wileyonlinelibrary.com).

© 2017 Wiley Periodicals, Inc.

might differentially contribute to NIRS signals across channels. Therefore, we newly applied a multivariate approach, a partial least squares regression, to explain NIRS signals with multivoxel information from fMRI within the brain and soft tissues in the head. We concurrently obtained fMRI and NIRS signals in 9 healthy human subjects engaging in an *n*-back task. The multivariate fMRI model was quite successfully able to predict the NIRS signals by cross-validation (interclass correlation coefficient = ~0.85). This result confirmed that fMRI and NIRS surely measure the same hemoglobin concentration. Additional application of Monte-Carlo permutation tests confirmed that the model surely reflects temporal and spatial hemodynamic information, not random noise. After this thorough validation, we calculated the ratios of the contributions of the brain and soft-tissue hemodynamics to the NIRS signals, and found that the contribution ratios were quite different across different NIRS channels in reality, presumably because of the structural complexity of the frontotemporal regions. *Hum Brain Mapp 38:5274–5291, 2017.* © 2017 Wiley Periodicals, Inc.

Key words: fMRI; NIRS; multivoxel pattern analysis; PLSR

INTRODUCTION

Near-infrared spectroscopy (NIRS) is a nonrestrictive, noninvasive brain mapping technique. It exploits the different optical absorption spectra of oxygenated and deoxygenated hemoglobin in the near-infrared region. Multiple pairs of probes, emitting and receiving near-infrared light, are attached to the scalp and topographically measure the absorption rates that should reflect the regional hemodynamics of the brain. NIRS has been increasingly used even in clinical settings for psychiatric diagnoses [Takizawa et al., 2014].

There are still many questions regarding the validity of the NIRS technique, however [Cyranoski, 2011]. Such critiques are based on the presence of inevitable contamination by blood flow in the soft tissues (STs) and the variability of optical path lengths across channels [Kirilina et al., 2012; Takahashi et al., 2011]. The hemodynamics in the gray matter (GM) and STs may be temporally correlated on average [Anderson et al., 2011]. Moreover, the anatomical complexity of the head may cause unexpected and irregular optical refractions, thus resulting in different absorption rates across different parts of the head.

Despite these technical issues, it is of critical importance to know the actual contribution of brain hemodynamics to the observed NIRS data in each measuring point or "channel"; furthermore, it is important to understand differences in the brain contributions across channels. These issues have not previously been clarified.

One way to validate the NIRS technique is by simultaneously performing both NIRS and functional magnetic resonance imaging (fMRI) [Cui et al., 2011; Sato et al., 2013]. fMRI is an established and widely used brain mapping method with high spatial resolution. However, a major problem is that the existing literature has shown considerable dissociation between observed NIRS signals and regional blood-oxygen-level-dependent (BOLD) signals. For example, low correlation coefficients have been observed, $r \sim 0.2$ on average, between BOLD and NIRS signals [Cui et al., 2011], especially in the frontal and temporal regions. Moderate correlations ($r \sim 0.4$–0.5) have been observed [Sasai et al., 2012; Sato et al., 2013] after examination of only a limited number of regions with robust task-related activation or best correlations. Therefore, how NIRS and brain BOLD signals consistently correlate across the whole set of available NIRS channels remains unclear, although both NIRS and BOLD should theoretically reflect identical hemoglobin concentrations. This discrepancy may occur because (1) the hemodynamics in STs confounds only NIRS data and (2) the structural complexity of the head causes different absorption rates of near-infrared light across MRI *voxel*s (millimeter-order unit volumes). Importantly, BOLD signals in different voxels have been "averaged" within a volume-of-interest (VOI) in most conventional correlation analyses between NIRS and BOLD, and this process may result in the loss of the complex NIRS-BOLD associations that differ across voxels.

Here, to validate NIRS data with concurrent BOLD measurements, we introduced a multivariate approach, focusing on spatially distributed multivoxel dispersions of activity [Kamitani and Tong, 2005]. Different rates of absorption of near-infrared light at different voxels should cumulatively produce a total absorption rate in a given NIRS "channel." This was modeled by linear regression for each NIRS channel, in which voxel-by-voxel BOLD signals were weighted differently and concatenated to explain the NIRS signal. A precise estimation of this exploratory model should divide the NIRS data into two components—one for cerebral cortices and one for STs. We adopted a partial least squares regression (PLSR) [Wold et al., 1984] to overcome the multicollinearity problem across many explanatory variables (specifically, many voxels containing BOLD time series).

MATERIALS AND METHODS

The authors declare that all experiments on human participants were conducted in accordance with the Declaration of Helsinki and that all procedures were carried out in participants who had adequate understanding of the procedures and provided written consent. The study was approved by

the Ethics Committee of National Center of Neurology and Psychiatry (Kodaira, Tokyo).

Participants

Eleven right-handed, healthy female volunteers (mean [SD] age = 28.0 [1.42] years, age range: 21–36 years) initially participated in this study. Only females were recruited because of their comparatively smaller head sizes, thus allowing for a space large enough to set the NIRS probes in a tight MRI head coil, and because of their comparatively smaller frontal sinuses [Lee et al., 2010]. None of the participants had a history of psychiatric or neurological disorders, head injury, or any medical drug use. Two participants were excluded from the analysis because of large motion artifacts in the data, thus resulting in a final sample of 9 females (mean [SD] age = 28.8 [1.61] years, age range": 21–36 years) whose data were analyzed.

NIRS Apparatus

For simultaneous NIRS–fMRI measurements, we used an optical topography system that is also used clinically for diagnostic purposes (ETG-4000, Hitachi Medical Corporation, Japan). The light sources consisted of continuous laser diodes with two wavelengths, 695 and 830 nm. The light was transmitted and detected by avalanche photodiodes whose initial sampling rate was 40 Hz, which was subsequently downsampled to 10 Hz. The near-infrared light was irradiated from source probes and was received by detecting probes attached to the skin of the forehead. Signals were transmitted through optical fibers that were attached to the probes. The participants wore a cap with the probe holder (Fig. 1a and b). We used a soft silicon probe holder that was customized for NIRS measurement in the MRI scanner, with 30 mm spacing between the source and the detector probes, covering the frontal and temporal head regions.

Eleven light sources and 11 detectors were embedded in the probe holder, arranged in a 2-vertical × 11-horizontal lattice pattern with 30 mm separation. Thirty-one vertical and horizontal pairs of source-detecting probes consisted of "channels," which measured point-to-point oxy-, deoxy-, and total-hemoglobin concentration changes. The probe holder was attached to the participants' foreheads. The most front-lower two probes were placed according to the line connecting Fp1 with Fp2 of the international 10–20 system for electroencephalography. The probes, optical fibers, and the holder were completely MRI compatible, and the pieces of the apparatus (including the coating material) were customized to avoid any artifacts on the MRI data. We placed MRI markers on the holder, one for each probe location, to provide sharp, distinct spot images on the T1-weighted MRI image so that the markers indicated the spatial positions (3D coordinates) of the probes in the MRI images. The channel formation averaged across participants is illustrated in Figure 1c.

Each participant had 31 channels, thus resulting in data from 279 channels for each of the oxy-, deoxy-, and total-Hb measures. However, we excluded data from 37, 27, and 26 channels for oxy-, deoxy-, and total-Hb and finally obtained data for the analyses from 242, 252, and 253 channels of oxy-, deoxy-, and total-Hb, respectively. This data exclusion was performed on the basis of the automatic process (Auto Gain, www.fda.gov/cdrh/510k/k042501.pdf) implemented in the NIRS hardware by using the criteria of signal credibility, such that data obtained with "under gain" should be excluded.

MRI Sequences

Image data were acquired using a Siemens Magnetom Verio 3-T whole body high-speed imaging device equipped for echo planar imaging (EPI) with a 12-channel gradient head coil (Siemens Medical Systems, Erlangen, Germany). Expandable foam cushions restricted head movement. After an automated scout image was acquired, and shimming procedures were performed to optimize the field homogeneity, we collected a T1-weighted 3D structural image by using a magnetization-prepared rapid gradient echo (MPRAGE) sequence with the following parameters: TR/TE/flip angle = 1900 ms/2.52 ms/7°, 256 × 256 matrix, in-plane resolution of 1.0 × 1.0 mm, and 1.0-mm sagittal slice thickness. For BOLD fMRI, the images were acquired using a gradient echo T2*-weighted EPI sequence (TR/TE/flip angle = 3.0 s/30 ms/90°, 96 × 96 matrix, in-plane resolution of 2.5 × 2.5 mm, and 3.13 mm transverse slice thickness). Both T1 and EPI images covered the whole brain and scalp. BOLD signals of the voxels in STs have already been used to explain NIRS signals in simultaneous measurements of fMRI and NIRS [Kirilina et al., 2012; Sato et al., 2013]. At the beginning of the EPI scanning, six volumes were acquired and discarded to allow the longitudinal magnetization to reach equilibrium.

Experimental Task in the Scanner

We used an *n*-back task, which has long been used to measure working memory performance. Our primary aim was to compare the fMRI and NIRS data by measuring the hemodynamics-related signals of both EPI and NIRS. Therefore, individual working memory performance was not actually of interest in our experiment. The *n*-back task was adopted only to elicit any robust hemodynamic changes in the frontotemporal areas, which are the focus of clinical diagnosis in psychiatry.

The participants observed visual stimuli and responded by pressing a button on an MRI-compatible response box: any one of 9 digits (1–9) was randomly displayed one-by-one, for 1.5 s each, and the participant was required to judge whether the current number matched the one from *n* steps earlier in the sequence (Fig. 2). The participants were asked to complete two kinds of *n*-back tasks: *2*-back and *1*-back. The *2*-back task was designed to engage more of the working memory resources than the *1*-back task so that subtracting the activity in the *1*-back task from that in the *2*-back task

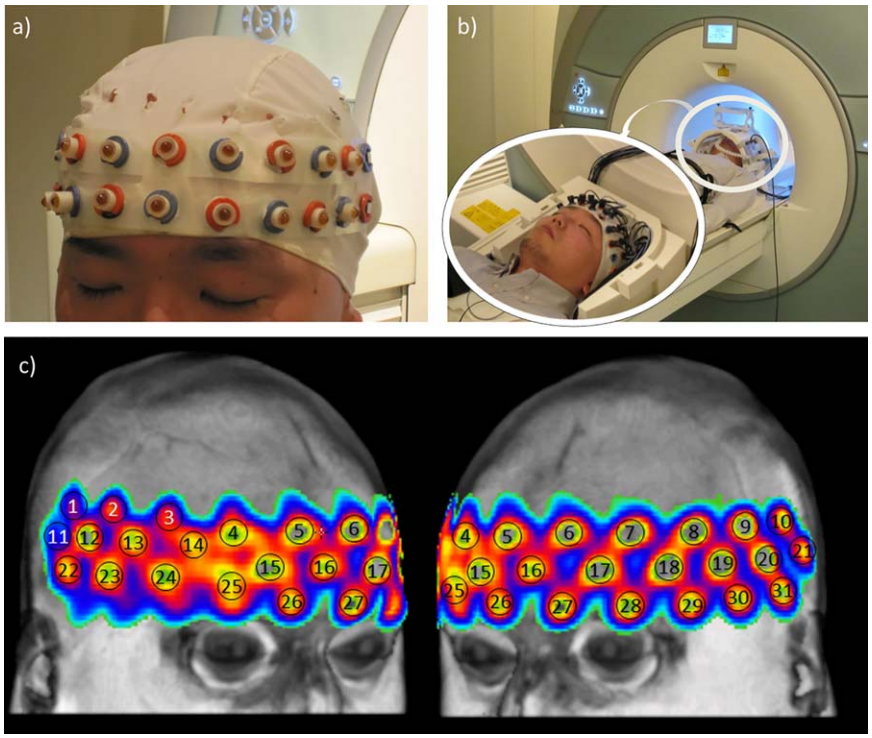

Figure 1.

Simultaneous NIRS–fMRI measurement. (a) The participants wore a cap with the probe holder. Any coating materials were not used in the pieces of the apparatus (because of the noise in the BOLD data), which resulted in the probe holder having a white color. Dark red spots show the probes (only for illustration purposes here). The probes encircled by red attachments indicate emitting probes, and the probes encircled by blue attachments indicate detecting probes. (b) A scene of NIRS–fMRI simultaneous measurement. The probes were attached onto the head in the MRI head coil. The optical lines to the NIRS device were placed neatly, avoiding forehead and temporal areas, to avoid perturbing the fMRI measurement of soft tissues. (c) The interparticipant averaged positions of the NIRS channels, warped, and rendered onto a normalized head image. Peaks with high probability are colored yellow and are numbered (Ch1–31). [Color figure can be viewed at wileyonlinelibrary.com]

produced a neural activation map associated with working memory performance, especially in the dorsolateral prefrontal area. Both the *2*-back and the *1*-back tasks started with a 1.5 s cue indicating the required task (such as "2-back" or "1-back"). Each epoch lasted for 30 s, including 19 presentations of the numbers. The entire session consisted of five iterations of a combination of a *2*-back epoch, a *1*-back epoch, and a 30 s rest (Fig. 2). During the rest period, the participants were instructed to simply look at a fixation cross in the display. The entire session lasted 7.5 min, during which we obtained 150 whole-brain EPI scans for each participant.

Data Analysis

Preprocessing of the fMRI data

We used SPM8 software (the Wellcome Trust Centre for Neuroimaging, http://www.fil.ion.ucl.ac.uk/spm). The images were adjusted for slice timing and were realigned to the first image of the run. The two T1-weighted structural volumes (with and without MRI markers indicating the probe locations) were spatially co-registered to the first functional image. For multivoxel analyses, the functional EPI images were not spatially normalized to a Montreal Neurological Institute (MNI) template because normalization degrades dispersed information in multivoxel BOLD signals. For conventional task-related GLM analyses, the EPI images were spatially normalized.

Segmentation of the structural MRI and identification of the GM and the ST

To identify individual cortex and ST locations, a participant's co-registered T1 image was classified and segmented into 6 different tissues (GM, white matter, cerebrospinal fluid, bone, ST, and air/background) using the New Segment toolbox in SPM8. The individual mask images were then created for GM and ST.

Localization of the voxels in a path of near-infrared light between an emitting and a receiving probe

We used the following photon-hitting density function [Feng et al., 1995] to identify the spatial distribution of the near-infrared light emitted and received by the two probes:

$$P_n(x,y,z)=\frac{z^2\exp\left(-k\left\{\left(x^2+y^2+z^2\right)^{\frac{1}{2}}+\left[(d-x)^2+y^2+z^2\right]^{\frac{1}{2}}\right\}\right)}{\left(x^2+y^2+z^2\right)^{\frac{3}{2}}\left[(d-x)^2+y^2+z^2\right]^{\frac{3}{2}}\times\left[k\left(x^2+y^2+z^2\right)^{\frac{1}{2}}+1\right]\left\{k\left[(d-x)^2+y^2+z^2\right]^{\frac{1}{2}}+1\right\}}.$$

In this equation, $P_n(x,y,z)$ represents the photon-hitting probability density per unit volume (= voxel) at the coordinate (x, y, z) (in mm) where a photon injected at (0, 0, 0) and detected at $(d, 0, 0)$ crosses. The coefficient k (the effective attenuation coefficient) is defined as $k=(3\mu_a\mu'_s)^{1/2}$, where μ_a is the absorption coefficient (0.011 mm^{-1}), and μ'_s is the reduced scattering coefficient of tissue (1.2 mm^{-1}) [Sassaroli et al., 2006; Sato et al., 2013]. We selected voxels with $P_n > 10^{-10}$ within the GM and ST masks obtained by the aforementioned segmentation process [Sato et al., 2013] and within newly created GM and ST masks that were theoretically "irradiated" by near-infrared light for each NIRS channel. We chose the threshold of $P_n > 10^{-10}$ because it had been used in a previous study [Sato et al., 2013], and a pilot analysis suggested that the difference in P_n did not substantially influence the results (data not shown, because this test is beyond the scope of this article).

Conventional task-related general linear model (GLM) analysis of fMRI and NIRS

To illustrate the conventional topological map of the activated areas by the *n*-back task, we used general linear model (GLM) analyses by SPM8. For the fMRI data, each EPI volume was spatially normalized to the MNI template space to enable the group analyses. We extracted all the voxels in the GM and the ST that were irradiated by the 31 pairs of source/detecting NIRS probes, using the aforementioned GM and ST masks produced by the photon-hitting function. The voxels formed two regions of interest, that is, the entire frontotemporal GM and ST. We applied voxel-by-voxel, intersubject GLM analyses to the two regions. We convolved the stimulus function model (a 30 s epoch in each *2*-back and *1*-back condition) with a canonical double-gamma hemodynamic response function and obtained a hypothetical delayed box-car hemodynamic model for each condition. The hemodynamic models for the *2*-back and *1*-back tasks and the 6 motion parameters from the realignment process were entered as the regressors in the GLM. We also applied a high-pass filter with a cutoff period of 128 s to the BOLD time series data. The data were temporally smoothed by an autoregressive model [AR(1)] implemented in SPM8. The maps of the

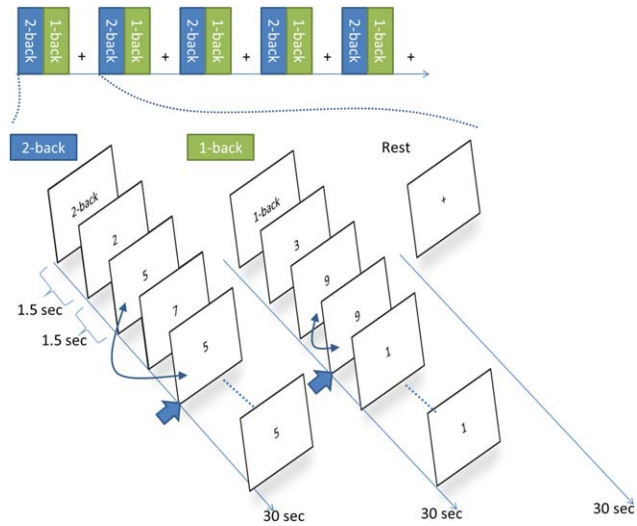

Figure 2.
The experimental task for the participants (*n*-back task). The *n*-back task consisted of blocks alternating *2*-back tasks and *1*-back tasks, followed by a rest period. The duration of each task was 30 s. The participants were required to press a button (blue thick arrows in the diagram) if they thought the observed number was the same as the one that had appeared *n* steps earlier. [Color figure can be viewed at wileyonlinelibrary.com]

estimated parameters (betas) for these regressors were then entered into a second-level, intersubject group analysis.

In the intersubject analyses, we obtained two types of topological maps as follows. For any general effects of the *n*-back task on brain activity, we performed *F*-tests in which the parameter estimates for both tasks (whether *2*-back or *1*-back) were compared with the rest condition. To inspect the differential effects of the *n*-back tasks more specifically, the individual map estimated for the *2*-back task was contrasted with the map for the *1*-back task. These contrasts were subsequently tested by a *t* test.

To produce the *n*-back activation map of NIRS, the time-series NIRS data in each channel were first resampled down to the same frequency as the BOLD time series (TR = 3 s). The NIRS data were then analyzed in the same way as the fMRI data to obtain the *F*-test map of "both tasks versus rest" and the *t*-test map of "*2*-back versus *1*-back." To illustrate the estimated values rendered on a head, each voxel within the GM mask beneath all 31 channels was filled with the *T* or the *F* value estimated for the NIRS channel nearest to that voxel, thus generating a 3D map of the estimation of the NIRS data.

We also verified the conventional bivariate correlations between the raw NIRS time series and the VOI-averaged BOLD time series ($r_{\mathrm{NIRS-BOLD}}$) in our data, including both brain and ST BOLD data. To account for different photon-hitting probabilities [Feng et al., 1995] in different voxels, weighted average was used for the BOLD time series data, with the photon-hitting probabilities as the voxel-by-voxel weights (i.e., the time series in each voxel was multiplied

by the probability relevant to that voxel, then all the data were averaged). We used this weighted average method by photon-hitting probabilities for all the BOLD data in the subsequent analyses.

Multivoxel analyses with partial least squares regression (PLSR)

Before the multivoxel analyses, the NIRS data were resampled down to the frequency of the BOLD time series (TR = 3 s).

Our model on the origin of NIRS signals is that the extent of access and the absorption rates of near-infrared light between an emitting probe and a receiving probe should be unpredictable on the basis of an *a priori* hypothesis and should be different between different voxels that cumulatively produce a total absorption rate in a given NIRS channel, which represents an aggregation of photon paths within both the brain and the STs between an emitting and a receiving probe. This scenario is modeled by linear regression for each NIRS channel:

$$Y_{nirs}=\sum_{v=1}^{k} b_v x_v+\sum_{v=k+1}^{n} b_v x_v+c+\varepsilon,$$

where Y_{nirs} represents the time-series data of NIRS that have been resampled to fit the sampling rate of BOLD (3 s), $v=[1,2,\ldots,k]$ and $v=[k+1,k+2,\ldots,n]$ represents the brain and ST voxels in each NIRS channel, respectively. x_v represents the BOLD time series at voxel v within the brain or STs [Sato et al., 2013], b_v represents the weight of voxel v, representing the absorption rate, c represents a constant, and ε represents the error (Fig. 3).

To compare the results with those from the multivoxel analysis, we also created a model based on the conventional bivariate approach using VOI-averaged data (weighted by the photon-hitting probability) as follows:

$$Y_{nirs}=b_{\mathrm{GM}}x_{\mathrm{GM}}+b_{\mathrm{ST}}x_{\mathrm{ST}}+c+\varepsilon,$$

where x_{GM} and x_{ST} represent the BOLD time-series averaged within the GM and ST VOIs, respectively. b_{GM} and b_{ST} represent the weights to be estimated, referring to the absorption rates in the GM and ST VOIs, respectively, when we average the voxel-by-voxel data within the VOI.

To estimate the two models that potentially explain the NIRS time-series data by multivoxel and VOI-based analyses of the BOLD data, respectively, we used a PLSR [Wold et al., 1984]. More specifically, we used the SIMPLS algorithm [de Jong, 1993] implemented in MATLAB® (Mathworks, Inc.).

The PLSR solves the simple linear problem. The model described above is rewritten as follows:

$$\mathbf{Y}=\sum_{v=1}^{n} b_v \boldsymbol{x}_v+c+\varepsilon,$$

where $\mathbf{Y}$ represents the time-series vector data of NIRS at a channel and $\boldsymbol{x}_v$ represents the time-series vector data of BOLD at voxel v within the tissues (including the ST and the cortex) (Fig. 4a). The equation can be further rescripted by using a design matrix $\mathbf{X}$ (concatenation of $\boldsymbol{x}_1, \boldsymbol{x}_2, \ldots \boldsymbol{x}_n$) and a weight vector $\boldsymbol{\beta}$ (a column vector formed by the concatenation of $b_1, b_2, \ldots b_n$) as follows (Fig. 4b):

$$\mathbf{Y}=\mathbf{X}\boldsymbol{\beta}$$

PLSR is a regression method that accounts for the "latent" structure in both datasets, $\mathbf{Y}$ and $\mathbf{X}$. It utilizes the covariance vector between $\mathbf{Y}$ and $\mathbf{X}$ ($\mathbf{X}^{\mathrm{T}}\mathbf{Y}$; both $\mathbf{Y}$ and $\mathbf{X}$ have been mean-centered to zero) and the iterative singular value decomposition (SVD) of this covariance vector [$\mathbf{X}^{\mathrm{T}}\mathbf{Y}=\mathbf{U}\Delta\mathbf{V}^{\mathrm{T}}(=\mathbf{U}\Delta$ if $\mathbf{Y}$ is a column vector)]. Here, $\mathbf{U}$ is an *orthonormal* matrix that has the same dimension as that of $\mathbf{X}$, and the vector Δ incorporates *singular values* that are arranged in descending order. Most importantly, the first singular vector $\mathbf{u}_1$ of $\mathbf{U}$ maximizes the covariation between $\mathbf{X}\mathbf{u}_1$ and $\mathbf{Y}$. Thus, $\mathbf{t}_1=\mathbf{X}\mathbf{u}_1$, which is called the "first latent" variable or the PLS score and best explains the variance of $\mathbf{Y}$. Therefore, we can use this $\mathbf{t}_1$ for the regression analysis, thar is, $\mathbf{Y}=b_1\mathbf{t}_1+\varepsilon$ (ε is the error term; see Fig. 4c). From this, we can obtain b_{w1} $(=\mathbf{t}_1^{\mathrm{T}}\mathbf{Y})$ for the first PLS score. The above process is conducted iteratively to estimate a series of b_{w1}, with a deflating $\mathbf{X}$ design matrix in each iteration such that the $\widehat{\mathbf{X}}_1$, a model matrix estimated by the first latent variable ($=\mathbf{t}_1^{\mathrm{T}}\mathbf{X}^{\mathrm{T}}\mathbf{t}_1$), is subtracted from $\mathbf{X}$ ($\mathbf{X}-\widehat{\mathbf{X}}_1$), and $\mathbf{X}$ is replaced with $\mathbf{X}-\widehat{\mathbf{X}}_1$, and $\mathbf{Y}$ is also replaced with $\mathbf{Y}-\widehat{\mathbf{Y}}_1$. In this way, PLSR finds a series of latent variables $\mathbf{t}_l$ such that the covariance between $\mathbf{t}_l$ and $\mathbf{Y}$ is maximized, and all $\mathbf{t}_l$ s are uncorrelated, thus providing z series of b_{w1} estimates (Fig. 4d). This process overcomes the collinearity problem arising from many independent variables of $\mathbf{X}$ and diminishes the variables' dimensions effectively. (For the methodological details of PLSR, see Abdi and Williams [2013].)

Validation of the PLSR fittings

To validate the fitting of the PLSR model, we calculated the mean squared prediction error (MSE), that is, the average of $\|\mathbf{Y}-\widehat{\mathbf{Y}}\|^2$, where $\mathbf{Y}$ is the actually observed NIRS time-series data, $\widehat{\mathbf{Y}}$ is the prediction by PLSR, and $\|\ \|^2$ is the square of the norm of a vector. To calculate the MSE, 10-fold cross-validation was used. The time-series data (150 time points in $\mathbf{Y}$ and $\mathbf{X}$) were randomly divided into 10 sets of 15, and the nine datasets were used to estimate the model, which was then tested on the remaining dataset $\mathbf{Y}$. The test was repeated 10 times on alternately different separations into training and testing datasets, and the mean MSE of the 10 tests was calculated. To confirm the stationarity across different validation methods, we added another validation method alongside the 10-fold cross-validation: a holdout validation in which the datasets were randomly separated into 3 sets of 50, with the two datasets used for training and the remaining one for one-time testing.

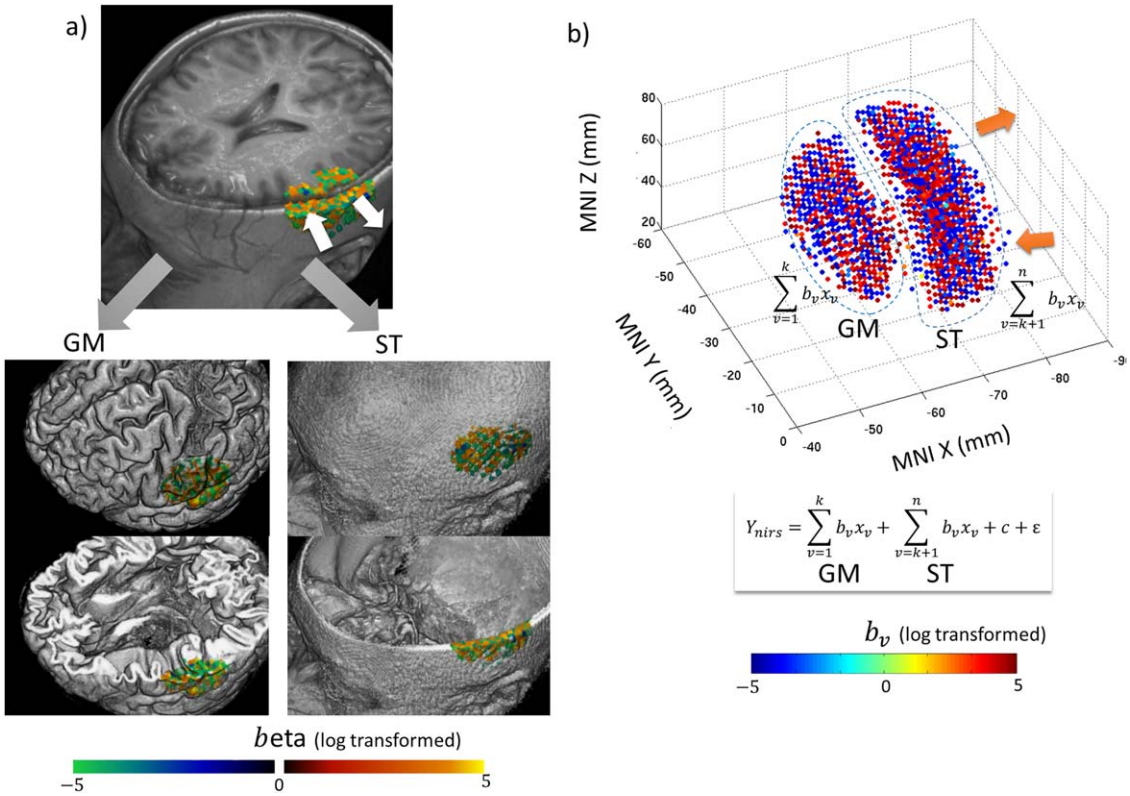

Figure 3.

An example of the distribution of the absorption rates (beta weights b in a regression model) in the cerebral cortex and soft tissues in a channel for a given participant. As described in the main text, different rates of absorption of near-infrared light at different voxels should cumulatively produce a total absorption rate Y_{NIRS} in a given NIRS channel as the equation in the figure, where $\sum_{v=1}^{k} b_v x_v$ denotes the gray-matter (GM) component and $\sum_{v=k+1}^{n} b_v x_v$ denotes the soft tissue (ST) component. (a) Voxel-by-voxel beta weights that should be estimated by the regression were rendered on the surface of the head, with grading colors indicating the beta values. On the top, two white arrows indicate the locations of an emitting probe and a receiving probe of near-infrared light. Through a segmentation method, the voxels that were selected by the aforementioned photon-hitting density function were parsed into those of GM (two lower left maps) and ST (two lower right maps). The beta weights (log transformed for illustration purpose) rendered on the cortical and soft-tissue surfaces show large variability from negative to positive values in a channel. (b) Beta weight distribution in a 3D MNI coordinate space [MNI X, Y, and Z (in mm)]. The two orange arrows indicate emitting and receiving probes, consisting of a channel or an aggregation of optical paths in both GM and ST (circled by dotted lines). The color bar indicates the value of the beta weights. The scatter plot shows the complex distribution of the beta weights (log transformed for illustration purpose), from negative to positive values. [Color figure can be viewed at wileyonlinelibrary.com]

One concern regarding PLSR fitting is "overfitting," meaning that even though the NIRS data were random and did not contain any information relevant to hemodynamics, multivoxel dispersions of the fMRI data might have falsely fit the random NIRS data. To exclude this possibility, we performed Monte Carlo permutation tests in which the NIRS time-series data in each channel were permuted randomly across the 150 time points and were fitted by multivoxel fMRI data using PLSR 1000 times (Fig. 5a). The histogram of 1000 prediction errors (MSE) provides a distribution that shows the probability density of the MSE. Each distribution was estimated by Kernel density estimation (KDE) with normal Gaussian kernels. With this probability density function, we were able to statistically test the null hypothesis that the MSE produced by PLSR fitting *without* any permutation occurs as a result of random chance.

We also evaluated whether NIRS and fMRI were *topologically* connected to each other. Theoretically, the NIRS data of a certain channel should be best explained by the multivoxel fMRI data located directly beneath that channel (hypothetically irradiated voxels between the two probes

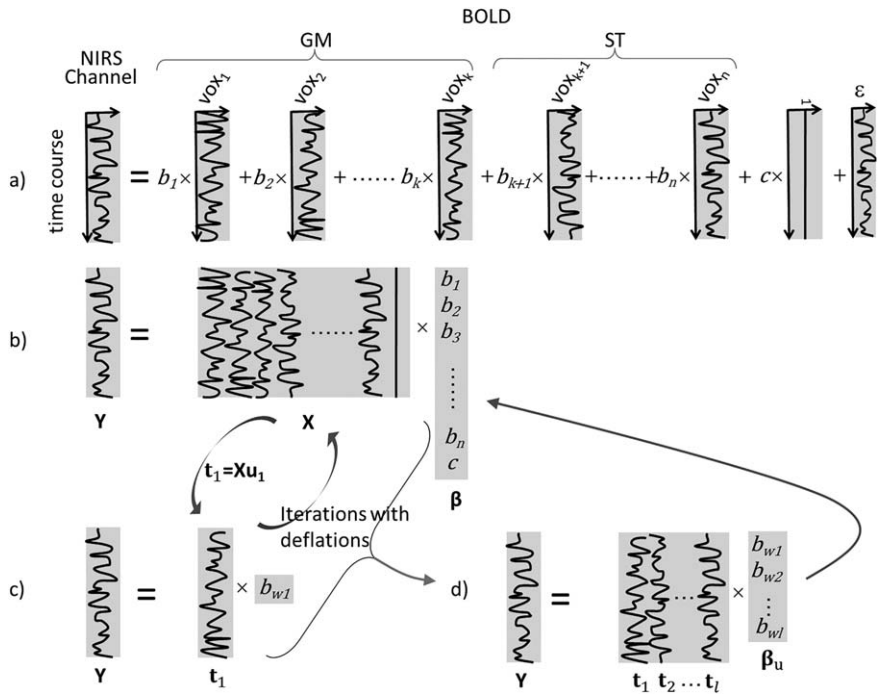

Figure 4.

Schematic representation of the PLSR procedure for the simultaneous measurement of NIRS-fMRI. (a) The NIRS time-series data in each channel can be explained by the linear combination of the "weighted" BOLD time series of every voxel (VOX) in the gray matter (GM; $1 - k$) and the soft tissue (ST; $k + 1 - n$) underneath the channel. b_i represents the beta weight in a voxel i, c represents a constant value, and ε represents an error term. (b) The matrix description of the linear regression model just described in (a). (c) The first singular vector $\mathbf{u}_1$ of the orthonormal matrix produced by singular vector decomposition of $\mathbf{X}$ maximizes the covariation between $\mathbf{t}_1 = \mathbf{X}\mathbf{u}_1$ ("first latent" variable or the PLS score) and $\mathbf{Y}$. This latent variable is used for the regression analysis on $\mathbf{Y}$, which produces an estimated parameter b_{w1}. (d) The process (b)–(c) is iterated l times, with deflation of $\mathbf{X}$ and $\mathbf{Y}$ in each iteration, and finally produces a series of b_w ($\boldsymbol{\beta}_u$), which is inversely rotated and turns into $\boldsymbol{\beta}$.

composing that channel) rather than by the fMRI data in any other remote region. To evaluate the topological consistency between fMRI and NIRS, we performed Mont-Carlo tests in which we permuted the combinations (pairings) of the NIRS data of 31 channels and 31 fMRI multivoxel datasets. For example, the NIRS data in one channel were paired with the fMRI data belonging to another remote channel (a schematic illustration is shown in Fig. 5b). For each iterative PLSR fitting, the NIRS datasets were paired with 31 fMRI datasets that were permuted randomly across the datasets. We repeated these PLSR fittings 1000 times on the basis of the "topologically false" matching of fMRI–NIRS pairing, thus producing 1000 MSEs (each of which was an MSE averaged across 31 channels). As in the case of time-series permutations, this process allowed us to calculate the probability of the prediction errors of fittings for the topologically correct pairing of fMRI–NIRS datasets among the distribution of the topologically randomized PLSR fittings.

Calculating the contribution of the GM hemodynamics to the NIRS data

After the validation of the PLSR fittings described earlier, we were able to obtain the following model in which the NIRS data in every channel are explained by multivoxel dispersions of the fMRI data:

$$\mathbf{Y}_{nirs} = \sum_{v=1}^{k} b_v \boldsymbol{x}_v + \sum_{v=k+1}^{n} b_v \boldsymbol{x}_v + \boldsymbol{c} + \varepsilon,$$

where $[v = 1, 2, \ldots, k]$ denotes the voxels in the GM mask and $[v = k + 1, k + 2, \ldots, n]$ denotes the voxels in the ST mask. Note that, if the prediction error ε is negligible, then the variation in the NIRS time-series data can be separated into variations of the GM and ST components. We calculated the time-series data of the GM and ST components in the equation. Then, we obtained a numerical contribution ratio (%) of the GM component to the NIRS data (Ctr_{GM}) by calculating the ratio of the magnitude of the variation (standard deviation [SD]) of the GM and ST time series.

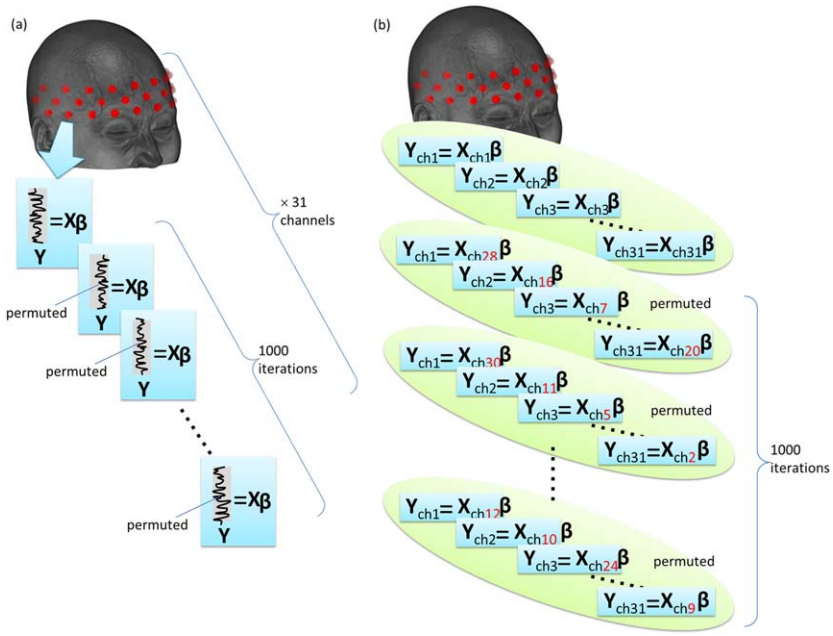

Figure 5.

Diagram of the Monte Carlo permutation test for the validation of the PLSR fitting. (a) Permutation of the temporal information. A regression analysis in each channel was repeated 1000 times with randomized permutations of the time series of the NIRS data. **Y** represents the NIRS time-series data, and **X** represents the BOLD time-series data across voxels underneath the channel. (b) Permutation of the spatial information. Parings of **Y** and **X** were permuted across 31 channels. PLSR regressions with such topologically permutated data were iterated 1000 times. [Color figure can be viewed at wileyonlinelibrary.com]

Evaluation of the bivariate correlations between the NIRS data and the averaged cortical BOLD data

In previous studies of the correlation between NIRS and BOLD, researchers have used bivariate correlation coefficients ($r_{\mathrm{NIRS-BOLD}}$) between NIRS and BOLD time-series data in the GM. To calculate the $r_{\mathrm{NIRS-BOLD}}$, however, multivoxel BOLD data are averaged across voxels in most cases so that such an approach may have discarded much of the information encoded in the multivariate pattern (e.g., the different and fine absorption rates of near-infrared light across voxels, as described earlier). If so, the conventional $r_{\mathrm{NIRS-BOLD}}$ in most cases should be lower than expected and should be relatively high only in a channel where the Ctr_{GM} is high because the NIRS data contain much information on cortical blood flow in that case. Therefore, we confirmed whether a correlation existed between the bivariate $r_{\mathrm{NIRS-BOLD}}$ and Ctr_{GM} across 31 channels in every participant.

RESULTS

Conventional Task-Related General Linear Model (GLM) Analysis of fMRI and NIRS

Before the multivariate analyses, we compared the canonical topological maps produced by fMRI and NIRS and confirmed a considerable difference in the spatial distribution of the signal changes even though the two measurements are based upon much the same hemodynamic changes (Fig. 6). We obtained BOLD activation maps from the contrast of 2-back minus *1*-back tasks, mainly involving the dorsolateral prefrontal cortices, which appeared to be typical for the working memory task [Owen et al., 2005] and the medial prefrontal area, which showed task-related deactivation [Mayer et al., 2010]. However, the NIRS-derived maps developed quite differently, such that medial prefrontal deactivation was not distinct, and the entire prefrontal region was positively activated. We also found that bivariate correlations between raw NIRS time series and VOI-averaged BOLD time series ($r_{\mathrm{NIRS-BOLD}}$) varied considerably across NIRS channels. On average, we did not find a correlation between the two datasets, thus resulting in means of $r_{\mathrm{NIRS-BOLD}} = 0.077$, -0.034, and 0.11 for oxy-, deoxy-, and total-Hb, respectively, which were not significantly different from 0 (Fig. 7). These two analyses suggested a dissociation between BOLD and NIRS data and a limitation of conventional bivariate correlations to match the BOLD and NIRS.

Multivoxel Analyses With Partial Least Squares Regression (PLSR)

In contrast, our new multivariate approach was able to attribute the NIRS time series to BOLD-derived multivoxel

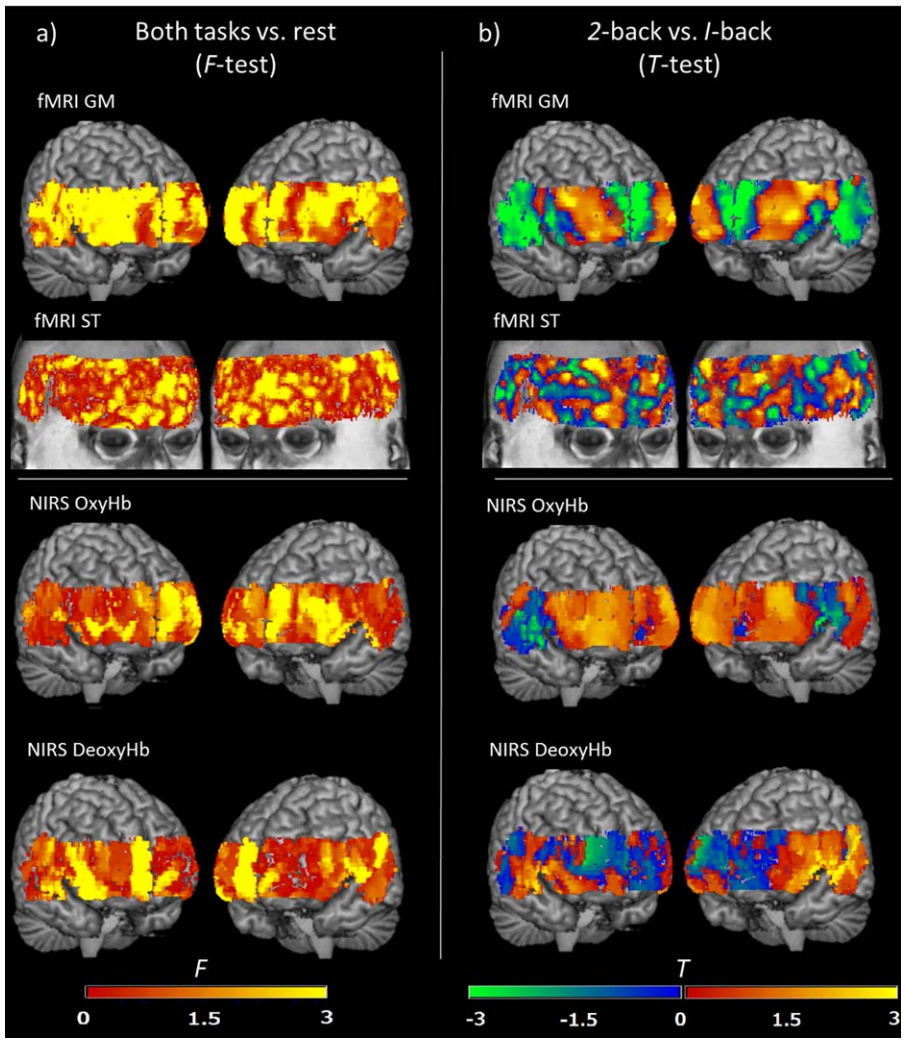

Figure 6.

Brain maps of parametric estimates by conventional GLM analyses of fMRI-BOLD (for gray matter [GM] and soft tissue [ST]), NIRS-oxyHb, and NIRS-deoxyHb across all the participants engaging in an *n*-back task. These maps indicate a large difference between BOLD and NIRS activation. (a) The statistical *F* maps show any differential effect of either the 2-back task (vs rest) or the *1*-back task (vs rest) by an *F*-test (both positive and negative effects included). (b) The statistical *T* maps show the differential effects of 2-back minus *1*-back. The fMRI maps show activation of the working memory in the lateral prefrontal cortices and task-related deactivation in midline structures around the frontal pole. The NIRS maps manifested quite differently such that oxyHb activation was more positively biased overall than fMRI. The BOLD-fMRI maps of soft tissues [the second row in (a) and (b)] indicate that there are non-negligible task-related effects on the hemodynamics in soft tissues. [Color figure can be viewed at wileyonlinelibrary.com]

dispersions in different tissue compartments within each NIRS channel. Plots of the observed NIRS data against the predicted data calculated by 10-fold cross-validation in every channel showed excellent consistency (Fig. 8). The class-2 interclass correlation coefficient (ICC_{2-1}) between all the observed and predicted data was 0.85 (0.79 with the additional holdout validation); thus, the multivoxel data explained, on average, 71.8% of the variance of the NIRS time series (62.4% with the holdout validation). Importantly, the prediction failed when we used a conventional VOI-averaged approach despite the inclusion of both GM and ST voxels in the model ($ICC_{2-1} = 0.36$, explaining only 12.7% of the variance of the NIRS time series on average [Fig. 9]) ($ICC_{2-1} = 0.24$ explaining 5.8% of variance using the holdout validation), thus indicating a clear advantage of the multivoxel approach. Note that the

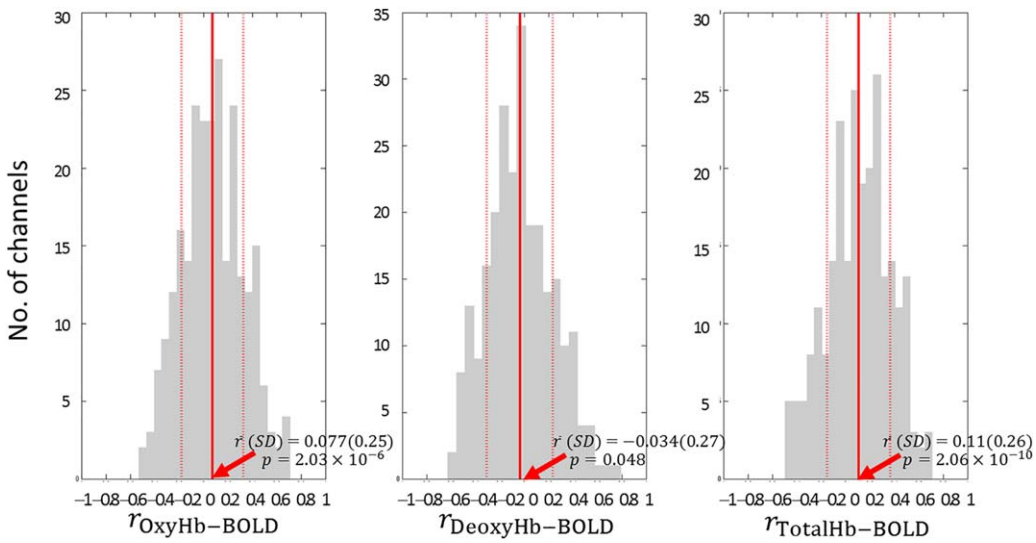

Figure 7.

The occurrence distribution of conventional temporal correlation between NIRS and VOI-averaged BOLD time series. In each NIRS channel in each participant, we calculated a correlation of raw NIRS time-series signals with the BOLD signals that were averaged across brain voxels within the channel (or VOI). The three gray histograms in the figure show the occurrence distribution (the number of channels) of such VOI-averaged correlation coefficients ($r_{\mathrm{NIRS-BOLD}}$) in all NIRS channels across all participants: correlations of VOI-averaged BOLD signals with oxy-Hb signals on the left ($r_{\mathrm{OxyHb-BOLD}}$), with deoxy-Hb signals in the middle ($r_{\mathrm{DeoxyHb-BOLD}}$), and with total-Hb signals on the right ($r_{\mathrm{TotalHb-BOLD}}$). A bold red line and two thin red-dotted lines indicate the mean correlation coefficient ($\bar{r}$) and the ±SD apart from $\bar{r}$, respectively. Although the three $\bar{r}$ values (centers of the distributions) are all statistically not equal to zero (see the *P* value below the $\bar{r}$ value), the sizes of $\bar{r}$ are quite small and close to 0 (0.077, −0.034, and 0.11 for oxy-, deoxy-, and total-Hb, respectively). The $r_{\mathrm{NIRS-BOLD}}$ varies considerably across different channels and the correlations are not strong on average, thus suggesting the inefficiency of using conventional VOI-averaged bivariate $r_{\mathrm{NIRS-BOLD}}$ to match BOLD with NIRS data. [Color figure can be viewed at wileyonlinelibrary.com]

average of the weights was around zero in each PLSR fitting (Fig. 10), showing that the weights did not relate to the VOI-based global signal changes, and the results of multivoxel analyses were difficult to visualize as smoothed "blobs" on the brain.

Validation of the PLSR Fittings

Such a precise multivariate model is sometimes the product of "overfitting," a process in which the model explains random error or noise rather than the underlying physiological relationship. To exclude this possibility, we developed Monte Carlo permutations to test the validity of the multivariate analyses by repeating "temporally false" PLSR fittings 1000 times with permutated NIRS time series (Fig. 5a), thus yielding a channel-by-channel random distribution of the predicting errors. As a result, the mean squared predicting errors (MSE) of the PLSR fittings on the NIRS data *without* any temporal randomization were located at the extreme low-side of the random distribution of the MSE ($P = 5.58 \times 10^{-129}$ across the participants [Fig. 11]). The results clearly showed that, by means of PLSR fittings, multivoxel BOLD dispersions correctly explained the temporal structure of NIRS rather than random error.

We also questioned whether NIRS and fMRI definitively shared "topological" information. We performed another Monte Carlo permutation test in which the NIRS time-series data in a certain channel were randomly fitted with multivoxel BOLD dispersions in a different channel, and these "topologically false" PLSR fittings were iterated 1000 times, thus producing a random distribution of MSE (Fig. 5b). The results showed that the probability of randomness of the fitting *without* any topological permutation was quite low within the distribution ($P = 0.0012$ [Fig. 12]). Although we had already observed substantial NIRS-BOLD differences in the activation maps (Fig. 6), the topological permutation verified that NIRS and BOLD data, including ST and brain data, shared topologically specific hemodynamic information combining brain and ST origins.

Calculating the Contribution of the GM Hemodynamics to the NIRS Data

Once we obtained the multivoxel model, we should be able to segregate the contributions of the brain and the

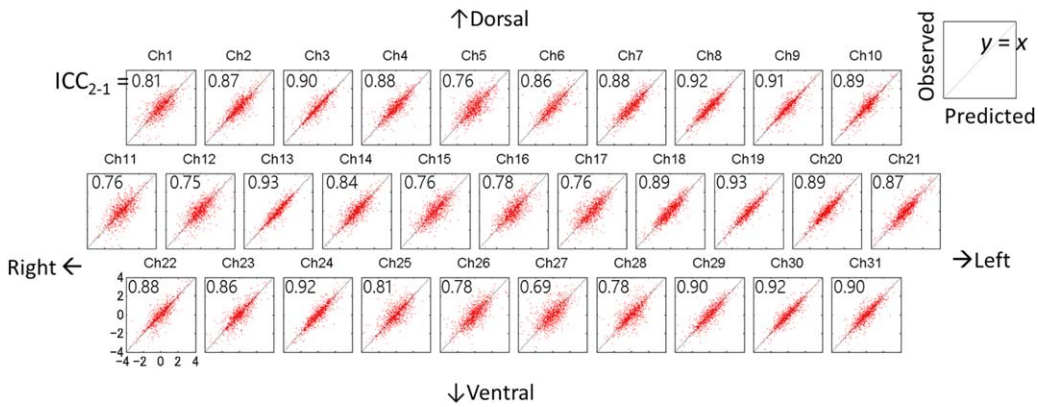

Figure 8.

Ten-fold cross-validation of PLSR fitting. Individual time-series BOLD and NIRS data were randomly classified into ten datasets; nine of those were used to estimate the PLSR model and the remaining dataset was used to test the model. Horizontal (x) and vertical (y) axes indicate the predicted and observed NIRS values, respectively. All the participants' results are superimposed on each plot channel-by-channel. The ICC_{2-1} between the predicted and the observed NIRS values is noted in each panel. The plotted dots mostly converge on the diagonal line $y = x$, indicating the high predictive power of PLSR. [Color figure can be viewed at wileyonlinelibrary.com]

STs from one another. Before the calculation, we confirmed that the time courses of the GM and ST components were highly correlated with the NIRS signals in every channel (Fig. 13). In the case of oxy-Hb, the averages (SD) of the correlation coefficients r across the 31 channels were 0.83 (0.11) and 0.80 (0.13), respectively, and the two correlation coefficients did not differ ($z = 0.34$, $P = 0.37$, a comparison of the two correlation coefficients). The results indicated that the temporal patterns of the GM and ST components were quite similar to the observed NIRS time course and that the two components that originated from multivoxel BOLD shared temporal information with the NIRS data. Thus, we were able to obtain the numerical contribution ratio (%) of the GM component to the NIRS data (Ctr_{GM}) by calculating the ratio of the magnitude of the variation (standard deviation [SD]) of the GM and ST time series.

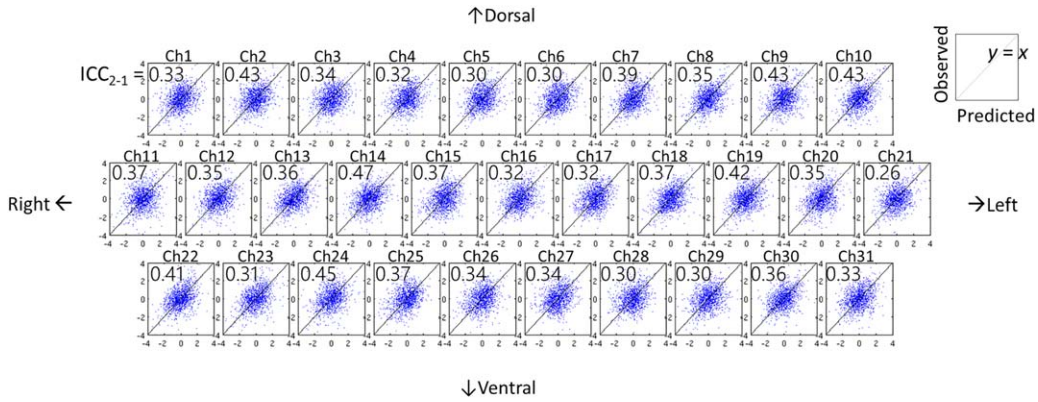

Figure 9.

Ten-fold cross-validation of regression with a conventional VOI-averaged approach. BOLD signals were averaged across the voxels in each channel (Ch) within each GM and ST VOI separately, thus producing two independent variables for PLSR, that is, VOI-averaged GM and ST time series of BOLD. The individual VOI-averaged time series of BOLD in the GM and ST and the time series of NIRS were randomly classified into ten datasets; of those, nine were used to estimate the PLSR model, and the remaining dataset was used to test the model. Horizontal (x) and vertical (y) axes indicate the predicted and observed NIRS values, respectively. All the participants' results are superimposed on each plot channel-by-channel. The ICC_{2-1} between the predicted and the observed NIRS values is noted in each panel. In contrast to the multivoxel approach (Fig. 8), the plotted dots here do not converge on the diagonal line $y = x$, thus indicating the low predictive power of PLSR when the BOLD data were averaged across voxels. [Color figure can be viewed at wileyonlinelibrary.com]

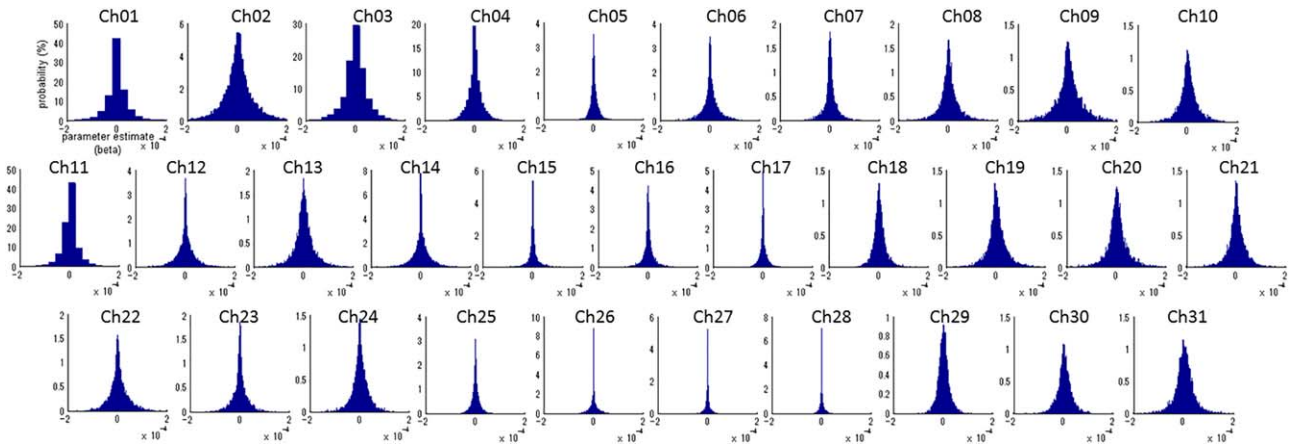

Figure 10.

Distribution of the parameter estimates of PLSR across the voxels in the VOI belonging to each channel. The horizontal axis indicates the values of parameter estimates assigned to the voxels and the vertical axis indicates probability. The graphs show that the parameter estimates by multivoxel PLSR in the voxels of each channel VOI distribute around zero symmetrically, regardless of the channel locations. [Color figure can be viewed at wileyonlinelibrary.com]

We found that the contribution ratios of GM (Ctr_{GM}) to the NIRS data varied substantially across the channels as shown in Figures 13 and 14. The Ctr_{GM} was high (up to 87%) in the dorsomedial frontal areas, but it was low (only ~20% in some channels) in the lateral (putatively corresponding to the temporal cortex) and lower frontopolar parts.

Evaluation of the Bivariate Correlations Between the NIRS Data and the Averaged Cortical BOLD Data

As described above, we already found a large variance in the conventional bivariate correlations ($r_{NIRS-BOLD}$) between the raw NIRS time series and the VOI-averaged BOLD time series (Fig. 7). The computation of Ctr_{GM}

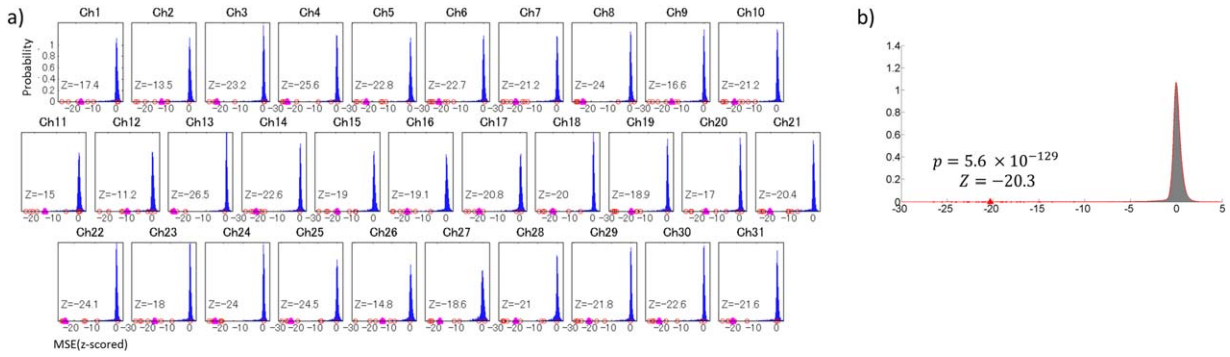

Figure 11.

(a) Monte-Carlo permutation test of the PLSR fittings of the time series across all participants. The PLSR fittings on NIRS by BOLD were iterated 1000 times for each channel, in which the NIRS data were randomly permuted across the time series in each iteration. This procedure produces the random distribution (blue histograms) of mean squared prediction errors (MSE). The horizontal axis in each channel indicates MSE, which has been standardized by participant. The vertical axis indicates the probability. The plots demonstrate that the MSEs in the PLSR *without* permutation (individual MSE [red circles], The MSE averaged across participants [magenta triangles], and the Z score for the averaged MSE [noted in the text]) are very small and are located far away from the mean of the random distribution (all the P values nearly equal 0), thus indicating that the PLSR fitting was surely based on correct information rather than random noise. (b) Intersubject results. The MSE *without* permutation (individual MSE [red dots] and MSE averaged across participants [red triangles]) is far small from the mean of the random distribution of the MSE (gray histogram). The figures illustrate oxy-Hb data, but the results were quite similar in the cases of deoxy- and total-Hb, which are not shown here. [Color figure can be viewed at wileyonlinelibrary.com]

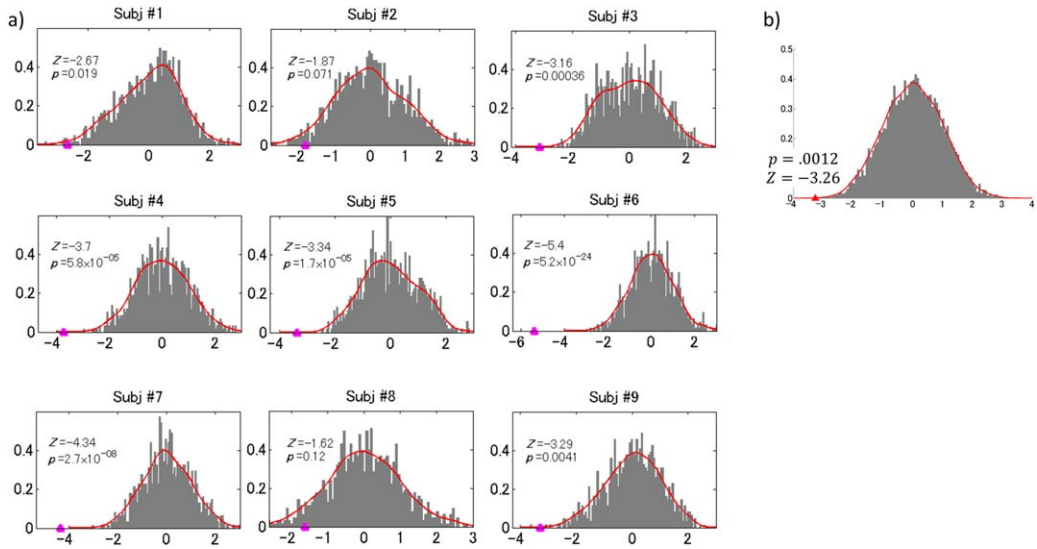

Figure 12.

(a) Individual Monte-Carlo permutation tests of PLSR fittings in terms of the "topological" relationship between NIRS channels and fMRI multivoxel datasets. The topological relationship between BOLD and NIRS data was randomly permuted across 31 channels, and the PLSR was iterated 1000 times. This produced a random distribution of MSE (gray histogram) for each participant (Subjects #1–#9). The horizontal axis in each channel indicates the individually standardized MSE, and the vertical axis indicates the probability. Each panel shows the probability of the random distribution of MSE, with a fitted Kernel probability density (KDE) function (red curve). The magenta triangles indicate the MSE *without* permutation. The results for most of the participants show significantly smaller MSE values within the random distribution. (b) Intersubject results. The MSE *without* permutation (MSE averaged across participants [red triangles]) is not far from the mean of the random distribution of MSE (gray histogram). The figures illustrate the case of oxy-Hb only, but the results were quite similar when we used deoxy- and total-Hb data. [Color figure can be viewed at wileyonlinelibrary.com]

further allowed us to explain this variability of $r_{\mathrm{NIRS-BOLD}}$, to some extent, because of a low but significant correlation between $r_{\mathrm{NIRS-BOLD}}$ and Ctr_{GM} across channels [$r(240) = 0.26$, $P = 3.1 \times 10^{-5}$ for oxy-Hb, $r(250) = -0.20$, $P = 0.0012$ for deoxy-Hb, $r(251) = 0.33$, $P = 7.7 \times 10^{-8}$ for total-Hb; Fig. 15] such that a lower conventional $r_{\mathrm{NIRS-BOLD}}$ at a channel is linked to a lower Ctr_{GM} at that channel.

DISCUSSION

The NIRS technique has already been applied to various neuroscientific questions by using oxy-hemoglobin concentration as a surrogate marker of neural/synaptic activity [Ferrari and Quaresima, 2012; Smith, 2011], although the users tend to ignore the fact that NIRS signals are inevitably confounded with nonbrain hemodynamic signals [Takahashi et al., 2011]. In fact, previous attempts of simultaneous fMRI–NIRS measurements have shown low correlations between BOLD and oxy-hemoglobin and have thus failed to validate NIRS as a brain mapping method [Cui et al., 2011], as replicated here. We observed substantial differences in the conventional topological maps between BOLD–fMRI and NIRS, and this discrepancy had not been clearly demonstrated in previous studies. The results of the *n*-back task, especially the *2*-back minus *1*-back contrast, showed that the present BOLD-based mapping replicated previous findings of activation in the lateral prefrontal areas [Owen et al., 2005] and task-related deactivation in the medial prefrontal area [Mayer et al., 2010]. However, NIRS-based mapping failed to show this contrast between the medial and lateral prefrontal areas. The overall positively biased activation maps of NIRS, especially the one derived from oxyhemoglobin, may have resulted from blood flow increases induced by task efforts in STs (the scalp and muscles) of the forehead region. Therefore, researchers should be aware that the channel-by-channel plain topological mapping of oxyhemoglobin changes must be interpreted with great caution.

In contrast to the discrepancy between plain topological maps, the PLSR-based multivoxel dispersions of both cortical and ST BOLD signals precisely predicted the time course and the spatial information of the NIRS data. PLSR is similar to principal component regression (PCR), which converges a multivoxel BOLD data matrix **X** into fewer orthogonal scores, as used in an fMRI study in combination with sparse estimation [Wager et al., 2013]. The crucial difference between PLSR and PCR is that PCR

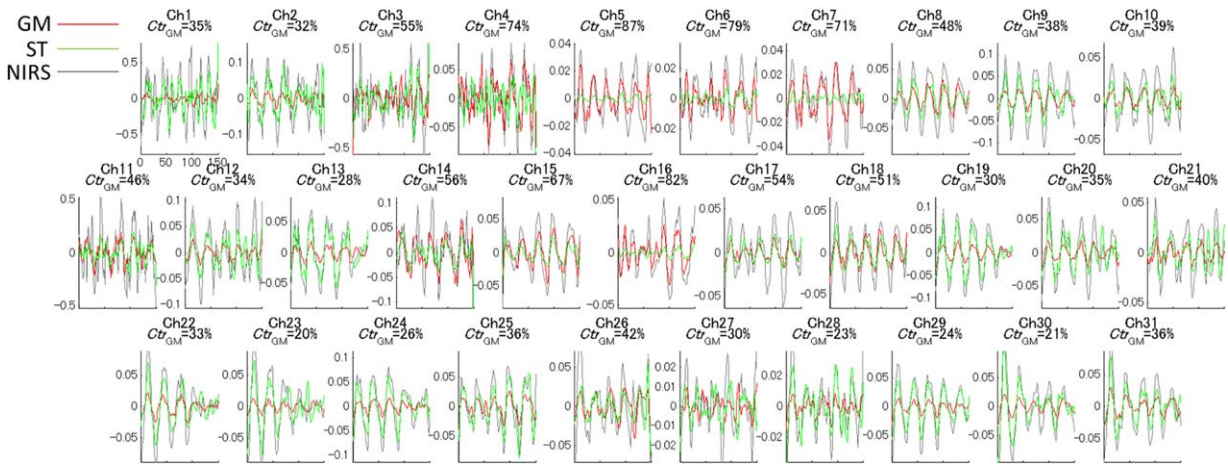

Figure 13.

The time course of oxyHb-NIRS across the entire session in each channel (Ch) and its GM and ST components. The vertical axes indicate signals (mean centered to zero). The gray line indicates the observed NIRS time course. The red line indicates the time course of the GM component estimated by PLSR, and the green line indicates the time course of the ST component. The time course in each channel shows periodical task-related activation, which reflects five iterations of the *2*-back and *1*-back tasks. The time course of oxy-Hb is highly correlated with that of the GM and ST components in every channel. The averages (SD) of the correlation coefficients *r* across 31 channels are 0.83 (0.11) and 0.80 (0.13), respectively, and the two correlation coefficients do not differ ($z = 0.34$, $P = 0.37$, a comparison of two correlation coefficients). The results indicate that the temporal patterns of the GM and ST components are quite similar to each other and to the observed NIRS time course and that the two components originating from multivoxel BOLD share temporal information with the NIRS data. Thus, we were able to obtain a numerical contribution ratio (%) of the gray-matter component to the NIRS data (Ctr_{GM}), as shown above the plotted panel in every channel. The pattern of Ctr_{GM} shows that the gray-matter contributions (red lines) are relatively dominant in more dorsal and medial parts of the frontal region. [Color figure can be viewed at wileyonlinelibrary.com]

considers only the variance of **X**, whereas PLSR considers the covariance of **X** and the dependent variable **Y**. PLSR had not previously been applied to an analysis of simultaneous fMRI–NIRS measurements, but it effectively decreased the dimension of multivoxel BOLD information, thereby explaining the NIRS signals and overcame the limit of the conventional bivariate correlation approach between NIRS and BOLD.

Note that the results of multivoxel analyses are difficult to visualize as smoothed "blobs" on the brain such as conventional brain mappings, such that estimated weights on the voxels are not necessarily related to the global activation averaged across voxels. In fact, the average of the weights was near zero in our study. This phenomenon has also been observed in other studies with multivoxel analyses of BOLD [Shibata et al., 2011]. A study comparing multivariate and conventional univariate analyses of task-related BOLD during a decision-making task [Jimura and Poldrack, 2012] has found that the two analyses showed largely segregated regions in explaining the variance of task-related performances. The authors have ascribed this difference to greater sensitivity of the multivariate analysis than the univariate analysis. This study has indicated that univariate and multivariate signals code different information and that multivariate data are more sensitive to explain a certain mental process. Consistently with those results, in this study, high-dimensional information coded as multivoxel BOLD dispersion precisely explained the time series and the spatial information of the hemodynamics of the NIRS data.

Multivoxel information is invisible and is difficult to illustrate as an intuitive brain map. Therefore, we confirmed the validity of the multivariate analyses by using Monte-Carlo permutation tests to ensure that the multivariate method appropriately modeled the temporal/spatial hemodynamic information of NIRS rather than random noise. The development of this new validation method of multivoxel analysis was one advantage of our method, thus eliminating overfitting, the most common issue in multivariate analyses.

The high predictive power and the spatial and temporal validity of our model shown in this study proved our hypothesis that the extent of access of the near-infrared light would be variable across different voxels and that the absorption rates would be different at different voxels in the head. Near-infrared light should be transmitted through multiple tissues with different refractive indices (such as the skin, extraocular and temporal muscles, skull

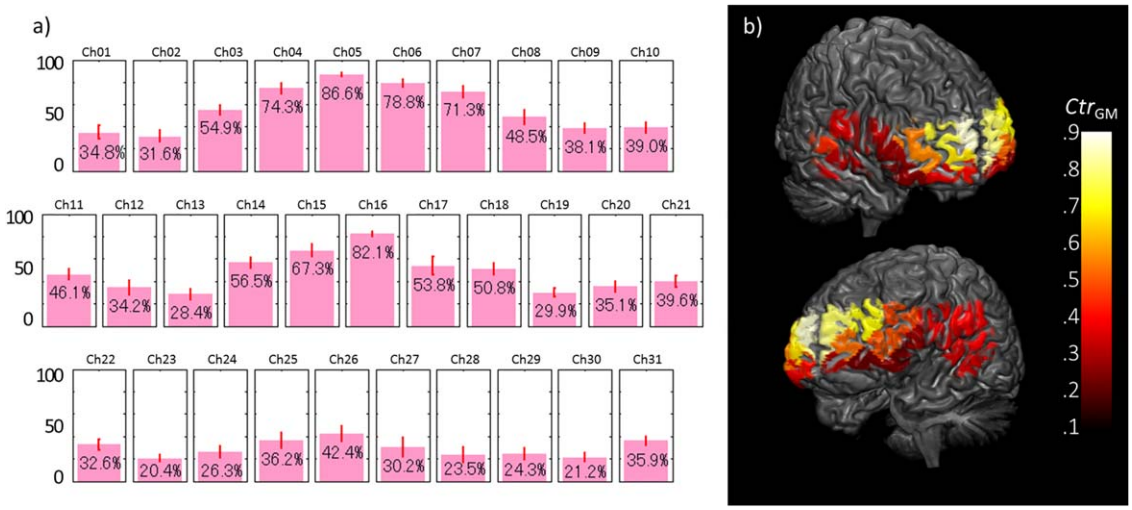

Figure 14.

Distribution of the gray-matter (GM) contributions to the NIRS time series. (a) The vertical axis indicates the estimated contribution ratio (%) of GM relative to the contributions of combined GM and soft tissue (Ctr_{GM}). The Ctr_{GM} varies significantly across channels (Ch) and is relatively high in the dorsomedial frontal part. The red error bars indicate the standard deviation across the participants. (b) The brain surface regions are colored differently according to the Ctr_{GM}. Each channel's Ctr_{GM} is projected with a relevant color onto the brain surface voxels nearest to that channel. The heat colormap bar shows the value of the Ctr_{GM} (from 0.1 to 0.9). The results of the Ctr_{GM} are based on the assumption that the PLSR model perfectly explains the NIRS time series. [Color figure can be viewed at wileyonlinelibrary.com]

bone, air within sinuses, cerebrospinal fluid, vessels, and cortex). Although a hypothetical model called photon-hitting density function [Feng et al., 1995] has already been proposed to identify the spatial distribution of near-infrared light, this model works only on the basis of the premise that the light travels through a homogenous space. The head region is spatially complex and is not at all homogeneous. This complexity should result in unexpectedly irregular and diffused refractions of optical paths in NIRS, thus making it difficult to hypothesize *a priori* optical paths.

The NIRS technique should reflect the concentrations of oxy- and deoxy-hemoglobin very accurately in an ideal situation without spatial complexity of the optical paths between NIRS probes, for example, testing an NIRS device using a dynamic phantom with an already-known structure [Okada et al., 1995; Sasai et al., 2012]. However, in reality, the structural complexity in the frontal and temporal head regions *in vivo* would substantially hamper measurements with NIRS unless NIRS could be combined with an individually tailored multilayered head model. In contrast, fMRI reflects spatial information in a straightforward manner: it detects BOLD effects (theoretically, the deoxy-hemoglobin concentration) with a spatial resolution of a few millimeters. This accuracy of fMRI in the detection of spatial information is not affected by the nuisance factors of NIRS such as the distance from the brain surface to the detectors and the multiple tissue layers in the head. However, BOLD itself may not simply reflect the concentration of deoxy-hemoglobin. In fact, associations of BOLD signals with hemoglobin concentration differ depending on the location of the voxel. For instance, the diameter of a vessel affects the relationship between the deoxy-hemoglobin concentration and BOLD; BOLD reflects deoxy-hemoglobin in large veins as expected, but in capillary-size vessels, BOLD reflects both oxy- and deoxy-hemoglobin [Ogawa et al., 1993; Yamamoto and Kato, 2002]. Another factor affecting the BOLD–hemoglobin relationship is the relative direction of the static magnetic field and the draining vein containing hemoglobin, such that the BOLD signal decreases as the direction of the magnetic field becomes more parallel to the draining vein [Yamamoto and Kato, 2002]. These factors are so influential that the correlation sometimes even "flips"—from negative to positive—between deoxy-hemoglobin and BOLD effects.

All these confounding factors, the contamination of NIRS signals from ST hemodynamics, the complex relationship between the hemoglobin concentration and BOLD signals, or both, should result in low correlation between NIRS data and VOI-averaged cortical BOLD signals. In brief, although both NIRS and BOLD measure the same hemoglobin concentration, NIRS data are not easily explained by BOLD data by using the conventional bivariate correlational approach. Instead, the possible variability of the association between near-infrared light and BOLD signals across different voxels was explained quite well by our multivoxel model, which resulted in the precise prediction of NIRS signals.

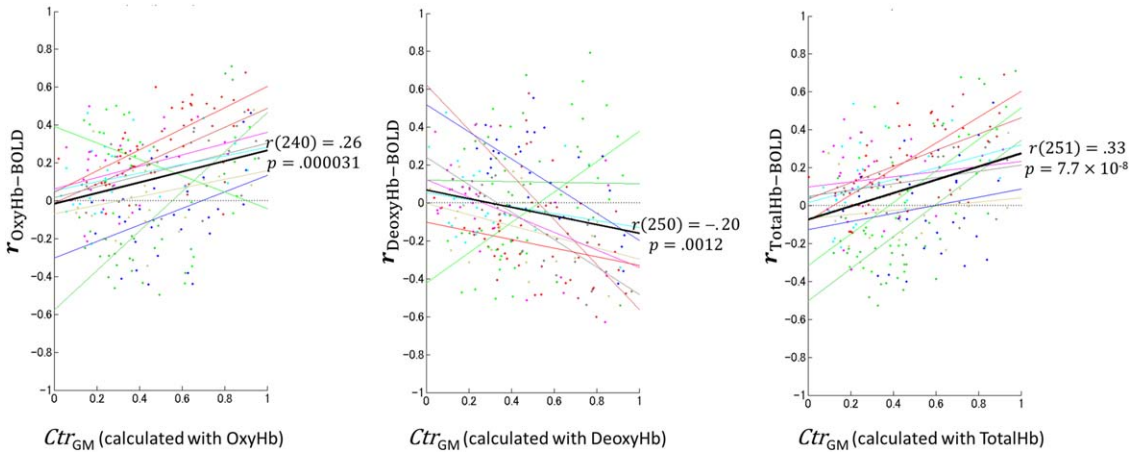

Figure 15.

The bivariate correlation between NIRS and spatially smoothed BOLD data ($r_{\mathrm{NIRS-BOLD}}$) and the contribution of the GM component to the NIRS data (Ctr_{GM}). Each dot indicates the datum in each channel in each participant. The different lines indicate fitted lines to the participant-level data, and different colors indicate different participants. Thick black lines indicate the fitted line to all the participants' data. The result in the case of oxy-Hb is shown in the left panel, deoxy-Hb is in the middle, and total-Hb is on the right. The horizontal axis indicates the Ctr_{GM}, and the vertical axis denotes $r_{\mathrm{NIRS-BOLD}}$. The plots show a significant association between $r_{\mathrm{NIRS-BOLD}}$ and Ctr_{GM} [the r and P values are noted beside the thick black fitted lines], such that a higher Ctr_{GM} in a channel tends to promote a stronger correlation between NIRS and BOLD data. [Color figure can be viewed at wileyonlinelibrary.com]

After we constructed the detailed model to explain NIRS data on the basis of BOLD signals, the proposed multivariate method finally allowed us to determine the contribution ratio of GM hemodynamics to the observed NIRS data in each channel. As a result, we found that the contribution Ctr_{GM} was substantially different between head regions, a reasonable result, given the aforementioned structural complexity of the frontal and temporal head. In particular, the Ctr_{GM} was low (only ~20% in some channels) in the lateral (temporal) and lower frontopolar parts, perhaps because of large temporal muscles in the lateral head and the frontal sinus and external ocular muscles affecting the NIRS signals. The results indicated that the simple mapping of bare NIRS data may not correctly reflect the spatial pattern of brain hemodynamics.

More importantly, the results also verified that NIRS signals in some parts of the forehead reflected brain hemodynamics fairly accurately, especially in the medial dorsal part, where the effects of the sinus and STs such as skin and muscle should be small. Some research studies have claimed that a major part of NIRS signals in the forehead is due to task-correlated blood flow changes in the skin (e.g., Takahashi et al. [2011]). Our findings clearly showed that NIRS can certainly detect hemodynamic changes in the frontal cortex if appropriate channels are selected. However, it is crucial to recognize that the variability of the cortical homodynamic contribution to NIRS signals depends on the regions and that the topographic distribution of oxyhemoglobin is currently difficult to interpret.

Finally, we propose that the observed low conventional bivariate correlations between NIRS data and VOI-averaged cortical BOLD data ($r_{\mathrm{NIRS-BOLD}}$) may be partly due to a low brain contribution. Additionally, as expected, we found a low but significant correlation between $r_{\mathrm{NIRS-BOLD}}$ and Ctr_{GM} across channels, such that part of the observed large variance of $r_{\mathrm{NIRS-BOLD}}$ was explained by the variance of Ctr_{GM}. This finding suggested that the previously reported low $r_{\mathrm{NIRS-BOLD}}$ was (e.g., Cui et al. [2011]), at least partly, due to low Ctr_{GM} in the selected channel. This analysis further supported the validity and the usefulness of our multivoxel approach and its product Ctr_{GM}.

This article has a limitation in that we tested our multivoxel approach only with a specific task-related activity (i.e., the n-back working memory task). Further studies are warranted to test whether the results obtained here might be applicable to other paradigms, such as other task-related activities, resting-state activities, and connectivity analyses.

CONCLUSION

We confirmed that NIRS unequivocally contains cortical hemodynamic responses as opposed to the idea that it merely reflects the blood flow of STs. However, given the large variability of GM contributions across NIRS channels, researchers must exercise caution when using NIRS as a topological mapping tool. The method proposed in this study to calculate different cortical contributions to

NIRS data is useful for the selection of channels in which signals correctly reflect brain hemodynamics and is expected to improve the NIRS technique as a valid tool for measuring brain functions in the future.

ACKNOWLEDGMENTS

We would like to thank Editage and Springer Nature Author Services for English language editing. This study was in part supported by the "Strategic Research Program for Brain Science of BMI Technologies for Clinical Application" and "Understanding of molecular and environmental bases for brain health" carried out under the Strategic Research Program for Brain Sciences and Brain Mapping by Integrated Neurotechnologies for Disease Studies (Brain/MINDS), Health Labor Science Research Grants from Japan Agency for Medical Research and development (AMED) and KAKENHI (26120008 and 16H03306) from MEXT, and the Intramural Research Grant for Neurological and Psychiatric Disorders of National Center of Neurology and Psychiatry, Japan, to TH.

CONFLICTS OF INTEREST

Hitachi Medical Corporation provided a project grant (JPY500,000 per year) and equipment support for this study, on the basis of a collaborative research contract between Hitachi Medical Corporation and National Center of Neurology and Psychiatry. T.N. of the National Center of Neurology and Psychiatry initiated this collaborative work and the contract with Hitachi Medical Corporation. S.K. is employed by Hitachi Medical Corporation.

REFERENCES

Abdi H, Williams LJ (2013): Partial least squares methods: Partial least squares correlation and partial least square regression. In: Reisfeld B, Mayeno AN, editors. Computational Toxicology: Volume II (Methods in Molecular Biology). New York, NY: Humana Press. pp 549–579.

Anderson JS, Druzgal TJ, Lopez-Larson M, Jeong EK, Desai K, Yurgelun-Todd D (2011): Network anticorrelations, global regression, and phase-shifted soft tissue correction. Hum Brain Mapp 32:919–934.

Cui X, Bray S, Bryant DM, Glover GH, Reiss AL (2011): A quantitative comparison of NIRS and fMRI across multiple cognitive tasks. NeuroImage 54:2808–2821.

Cyranoski D (2011): Neuroscience: Thought experiment. Nature 469:148–149.

de Jong S (1993): SIMPLS: An alternative approach to partial least squares regression. Chemomet Intell Lab Syst 18:251–263.

Feng S, Zeng FA, Chance B (1995): Photon migration in the presence of a single defect: A perturbation analysis. Appl Opt 34: 3826–3837.

Ferrari M, Quaresima V (2012): A brief review on the history of human functional near-infrared spectroscopy (fNIRS) development and fields of application. NeuroImage 63:921–935.

Jimura K, Poldrack RA (2012): Analyses of regional-average activation and multivoxel pattern information tell complementary stories. Neuropsychologia 50:544–552.

Kamitani Y, Tong F (2005): Decoding the visual and subjective contents of the human brain. Nat Neurosci 8:679–685.

Kirilina E, Jelzow A, Heine A, Niessing M, Wabnitz H, Bruhl R, Ittermann B, Jacobs AM, Tachtsidis I (2012): The physiological origin of task-evoked systemic artefacts in functional near infrared spectroscopy. NeuroImage 61:70–81.

Lee MK, Sakai O, Spiegel JH (2010): CT measurement of the frontal sinus - gender differences and implications for frontal cranioplasty. J Craniomaxillofac Surg 38:494–500.

Mayer JS, Roebroeck A, Maurer K, Linden DE (2010): Specialization in the default mode: Task-induced brain deactivations dissociate between visual working memory and attention. Hum Brain Mapp 31:126–139.

Ogawa S, Menon RS, Tank DW, Kim SG, Merkle H, Ellermann JM, Ugurbil K (1993): Functional brain mapping by blood oxygenation level-dependent contrast magnetic resonance imaging. A comparison of signal characteristics with a biophysical model. Biophys J 64:803–812.

Okada E, Firbank M, Delpy DT (1995): The effect of overlying tissue on the spatial sensitivity profile of near-infrared spectroscopy. Phys Med Biol 40:2093–2108.

Owen AM, McMillan KM, Laird AR, Bullmore E (2005): N-back working memory paradigm: A meta-analysis of normative functional neuroimaging studies. Hum Brain Mapp 25:46–59.

Sasai S, Homae F, Watanabe H, Sasaki AT, Tanabe HC, Sadato N, Taga G (2012): A NIRS-fMRI study of resting state network. NeuroImage 63:179–193.

Sassaroli A, de BFB, Tong Y, Renshaw PF, Fantini S (2006): Spatially weighted BOLD signal for comparison of functional magnetic resonance imaging and near-infrared imaging of the brain. NeuroImage 33:505–514.

Sato H, Yahata N, Funane T, Takizawa R, Katura T, Atsumori H, Nishimura Y, Kinoshita A, Kiguchi M, Koizumi H, Fukuda M, Kasai K (2013): A NIRS-fMRI investigation of prefrontal cortex activity during a working memory task. NeuroImage 83:158–173.

Shibata K, Watanabe T, Sasaki Y, Kawato M (2011): Perceptual learning incepted by decoded fMRI neurofeedback without stimulus presentation. Science 334:1413–1415.

Smith M (2011): Shedding light on the adult brain: A review of the clinical applications of near-infrared spectroscopy. Philos Trans Seri A Math Phys Eng Sci 369:4452–4469.

Takahashi T, Takikawa Y, Kawagoe R, Shibuya S, Iwano T, Kitazawa S (2011): Influence of skin blood flow on near-infrared spectroscopy signals measured on the forehead during a verbal fluency task. NeuroImage 57:991–1002.

Takizawa R, Fukuda M, Kawasaki S, Kasai K, Mimura M, Pu S, Noda T, Niwa S, Okazaki Y (2014): Neuroimaging-aided differential diagnosis of the depressive state. NeuroImage 85 Pt 1: 498–507.

Wager TD, Atlas LY, Lindquist MA, Roy M, Woo CW, Kross E (2013): An fMRI-based neurologic signature of physical pain. N Engl J Med 368:1388–1397.

Wold S, Ruhe A, Wold H, Dunn IW (1984): The collinearity problem in linear regression. The partial least squares (PLS) approach to generalized inverses. SIAM J Sci Stat Comput 5:735–743.

Yamamoto T, Kato T (2002): Paradoxical correlation between signal in functional magnetic resonance imaging and deoxygenated haemoglobin content in capillaries: A new theoretical explanation. Phys Med Biol 47:1121–1141.